Cell Reports
Physical Science

CellPress
OPEN ACCESS

Article

Lithium-ion hopping weakens thermal stability of $LiPF_6$ carbonate electrolytes

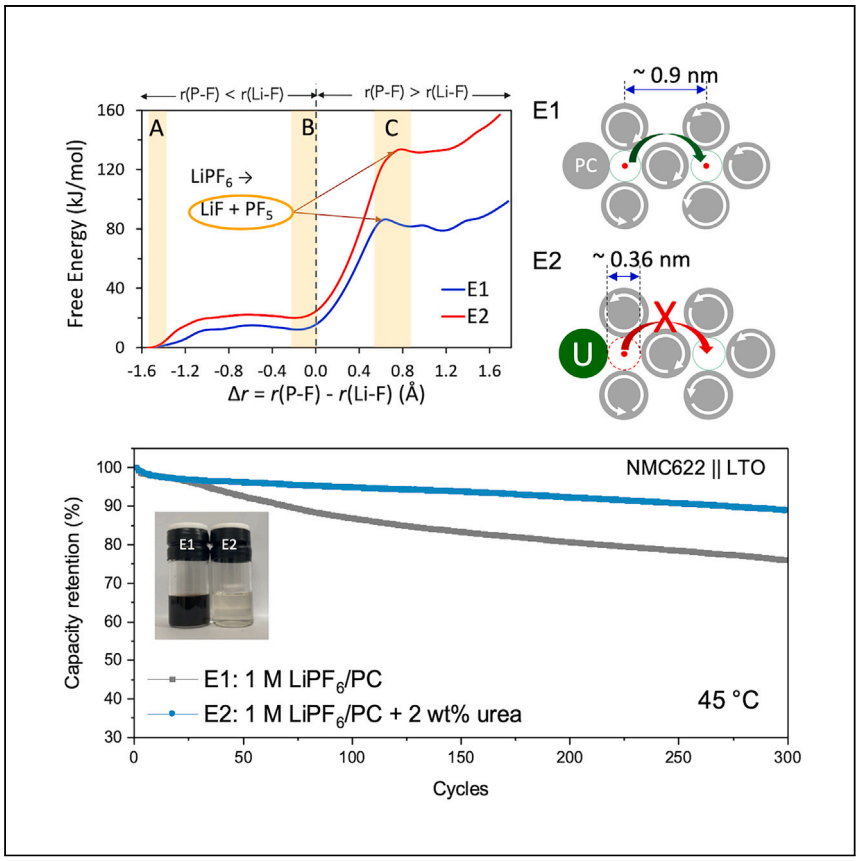

Han and Lee et al. demonstrate lithium-ion hopping induced by the overall reorientation of carbonate molecules is responsible for thermal instability of $LiPF_6$ carbonate electrolytes. Thermally stabilized $LiPF_6$ carbonate electrolytes, via preserving the vehicular transport of lithium ions, can improve calendar and cycle life of lithium-ion batteries at elevated temperatures.

Kee Sung Han, Mal-Soon Lee, Namhyung Kim, ..., GiovanniMaria Piccini, Roger Rousseau, Edwin C. Thomsen

keesung.han@pnnl.gov (K.S.H.)
malsoon.lee@pnnl.gov (M.-S.L.)

Highlights

Carbonate solvents experience overall rotational motion at elevated temperatures

Overall rotation of carbonate solvents is responsible for lithium-ion hopping

Suppression of lithium-ion hopping improves stability of $LiPF_6$ carbonate electrolytes

Thermally stabilized electrolyte enhances calendar and cycle life of lithium-ion batteries

Han et al., Cell Reports Physical Science 5, 101768
January 17, 2024
https://doi.org/10.1016/j.xcrp.2023.101768

Cell Reports
Physical Science

CellPress
OPEN ACCESS

Article

Lithium-ion hopping weakens thermal stability of $LiPF_6$ carbonate electrolytes

Kee Sung Han,[1,2,9,10,*] Mal-Soon Lee,[1,9,*] Namhyung Kim,[3,4] Daiwon Choi,[3] Sujong Chae,[3,5] Jaegeon Ryu,[3,6] GiovanniMaria Piccini,[1,7] Roger Rousseau,[1,8] and Edwin C. Thomsen[3]

SUMMARY

Lithium hexafluorophosphate ($LiPF_6$)-based carbonate electrolytes are widely used in commercial lithium-ion batteries (LIBs), but their thermal instability limits the cycle life and safety of LIBs at elevated temperatures. Few studies have yielded insight into the initial PF_6^- decomposition reaction that promotes thermal instability of $LiPF_6$-based electrolytes. Here, we find that lithium-ion hopping assisted by the overall reorientational motion of propylene carbonate molecules facilitates PF_6^- decomposition at elevated temperatures in 1 M $LiPF_6$/propylene carbonate electrolyte. Further, we demonstrate that urea additives, by preventing lithium-ion hopping, suppress the initial $LiPF_6$ decomposition reaction and enhance the thermal stability of the electrolyte. LIB cell tests with $LiNi_{0.6}Mn_{0.2}Co_{0.2}O_2$||$Li_4Ti_5O_{12}$ show improved LIB performance at elevated temperatures with the thermally stabilized electrolyte. This study provides key insights into the design of thermally stable $LiPF_6$-based carbonate electrolytes for improving the cycle life, calendar life, and safety of LIBs in elevated-temperature applications.

INTRODUCTION

Lithium hexafluorophosphate, $LiPF_6$, is widely used as a primary lithium salt in carbonate electrolytes for commercial lithium-ion batteries (LIBs) because of its favorable overall performance compared to alternatives.[1] One area in which $LiPF_6$-based electrolytes do not perform favorably, however, is thermal stability; thermal instability of LIBs limits both cycle life and safety.[1–3] Many attempts have been made to mitigate the thermal degradation from the electrolyte side reaction by coating or doping hetero-elements onto electrode materials.[4] Further, because lithium loss (the main cause of battery degradation) is a result of electrolyte interaction with other components,[3,5–9] alternative electrolytes have been considered for high-temperature LIBs.[10] Many studies have investigated thermal decomposition phenomena in $LiPF_6$-based carbonate electrolytes, primarily focused on decomposition pathways,[11–15] and they revealed that PF_5 (the product of the endothermic decomposition reaction $LiPF_6 \rightarrow LiF + PF_5$) is responsible for the subsequent decomposition reactions.[14,16] One attempt to mitigate decomposition used Lewis basic additives to form complexes with the Lewis acidic PF_5, trapping PF_5 to prevent subsequent reactions. Although this improved the thermal stability of the electrolyte, it did not diminish the loss of battery capacity at elevated temperatures due to the apparent reaction of the electrolyte to the electrodes.[17] Then it seems that the best way to boost the thermal stability of $LiPF_6$-containing electrolyte and LIBs is the suppression of PF_5 generation. Little is known about why PF_6^- decomposition occurs at elevated temperatures ($\geq 80°C$) in $LiPF_6$-based carbonate electrolytes.

[1]Physical and Computational Sciences Directorate, Pacific Northwest National Laboratory, Richland, WA 99352, USA

[2]Joint Center for Energy Storage Research, Pacific Northwest National Laboratory, Richland, WA 99352, USA

[3]Energy and Environment Directorate, Pacific Northwest National Laboratory, Richland, WA 99352, USA

[4]Present address: Department of Materials System Engineering, Pukyong National University, 45 Yongso-ro, Nam-gu, Busan 48513, Republic of Korea

[5]Present address: Department of Industrial Chemistry, Pukyong National University, 45 Yongso-ro, Nam-gu, Busan 48513, Republic of Korea

[6]Present address: Department of Chemical and Biomolecular Engineering, Sogang University, 35 Baekbeom-ro, Mapo-gu, Seoul 04107, Republic of Korea

[7]Present address: Department of Chemical and Geological Sciences, University of Modena and Reggio Emilia, Via G. Campi 103, 41125 Modena, Italy

[8]Present address: Chemical Sciences Division, Oak Ridge National Laboratory, Oak Ridge, TN 37830, USA

[9]These authors contributed equally

[10]Lead contact

*Correspondence: keesung.han@pnnl.gov (K.S.H.), malsoon.lee@pnnl.gov (M.-S.L.)

https://doi.org/10.1016/j.xcrp.2023.101768

However, it is noteworthy that $LiPF_6$ hydrolysis and the following decomposition reactions are much slower in aqueous solutions than in organic carbonate solutions containing residual water because of the strong ability of water to facilitate salt dissociation.[11,18] Based on the above observations, we hypothesize that $LiPF_6$ decomposition at elevated temperatures in carbonate solutions is due to changes in both the Li^+ solvation structure and the dynamic properties of the electrolyte components. It follows from this hypothesis that the thermal stability of LIBs could be improved by enhancing the thermal stability of the electrolyte via preventing $LiPF_6$ decomposition through stabilization of Li^+ solvation clusters by utilizing additives.[19] To verify the above hypothesis, we added a small amount (2 wt %) of urea into the electrolyte, 1 M $LiPF_6$ dissolved in propylene carbonate (1 M $LiPF_6$/PC, the number ratio of Li/PC/urea ≈1.0/11.8/0.4) due to its ability to affiliate lithium ion and carbonyl structure in common with carbonate solvents[20] and confirmed that this additive suppresses thermal decomposition of the electrolyte at 80°C (Figure S1). We investigated temperature-dependent rotational and translational dynamics and correlated lithium solvation structures and then lithium-ion transport mechanisms, in 1 M $LiPF_6$/PC with (E2) and without (E1) 2 wt % urea by using nuclear magnetic resonance (NMR) relaxation and pulsed-field gradient (PFG) NMR measurements in conjunction with ab initio molecular dynamics (AIMD) simulations combined with metadynamics calculations. In addition, to verify that E2 is practical in real applications, we tested cyclability and storage effects at elevated temperature (45°C) with $LiNi_{0.6}Mn_{0.2}Co_{0.2}O_2||Li_4Ti_5O_{12}$ (NMC||LTO) cells.

Here, we demonstrate that lithium-ion hopping assisted by overall reorientational motion of PC solvent molecules is responsible for initializing decomposition of PF_6^- in carbonate-based electrolytes at elevated temperatures. Urea additives stabilized Li^+ solvation clusters and successfully suppressed lithium-ion hopping via their preferential interaction with lithium ions, thereby suppressing thermal decomposition of the electrolyte. Battery performance, in both cycle life and capacity after storage at elevated temperatures, was noticeably improved by using the more thermally stable urea-added electrolyte. Based on this insight, thermal stability of LIBs can be efficiently improved without additional modification of electrode materials by simply adding Li^+ holding agents to suppress Li^+ hopping at elevated temperatures. Our findings present new opportunities for long-term storage and high-temperature applications of conventional, well-developed, ambient-temperature LIB chemistry.

RESULTS AND DISCUSSION

Li^+ transport mechanism and solvent dynamics

To elucidate the Li^+ transport mechanism, temperature-dependent diffusion coefficients (D) and spin-lattice (T_1) relaxation times were measured. Temperature-dependent D of E1 and E2 (Figure S2) showed $D_{Li} < D_{PF6} < D_{PC}$ for all measured temperatures, with little variation due to the presence of urea (Table S1). The fitting parameter $D_{0,Li}$ from the Vogel-Fulcher-Tammann (VFT) equation, $D = D_0 \cdot \exp(-B/(T-T_0))$, became the highest ($D_{0,PF6} < D_{0,PC} < D_{0,Li}$) in E1 but the smallest ($D_{0,Li} < D_{0,PF6} < D_{0,PC}$) in E2 due to strong coupling of urea toward Li^+[20–22] that resulted in $D_{urea} \approx D_{Li}$ (Figure S2), suggesting that the long-range Li^+ transport mechanism in E1 is different at higher temperatures than the low-temperature vehicular transport mechanism,[23] and that the urea additive helps to maintain vehicular transport of Li^+ even in higher temperatures. For a detailed analysis of the Li^+ transport mechanism, we explored the rotational dynamics of Li^+, PF_6^-, and PC across the samples E0 (pure PC), E1, and E2 from temperature-dependent ^7Li, ^{19}F, and ^1H T_1

(Figures 1A–1C). We found that the ^{1}H T_1 and ^{19}F T_1 behaviors did not vary significantly due to urea, while the ^{7}Li T_1 of E2 was strongly coupled with ^{1}H T_1 of urea, confirming the strong interaction of urea with Li^+. From the measured T_1 and D, we calculated rotational correlation time, τ_c, and overall reorientational correlation time, τ_2, which are correlated with the rotation of 1 and 2π radians, respectively (see experimental procedures). $\tau_{c,PC}$ (Figure 1D) and $\tau_{2,PC}$ (Figure 1E) noticeably increased due to the addition of $LiPF_6$ but did not change much due to urea, reflecting that urea additives minimally affect the PC solvent molecules. All τ_cs in E0, E1, and E2 but $\tau_{c,Li}$ and $\tau_{c,urea}$ in E2 abruptly jumped to the higher τ_c values at $T \approx 80°C$ (Figure 1D) due to the presence of the high-temperature $T_{1,min}$ (Figures 1A–1C), while τ_2 gradually decreased without such discontinuities (Figure 1E). Using τ_c and τ_2, the rotational flip angles, θ, for each electrolyte component were calculated (see experimental procedures) and plotted in Figure 1F. For PC and PF_6^-, θ values were gradually increased with the increase of temperature and abruptly jumped to greater than 360° at ~80°C (the data $\theta > 360°$ are not shown in the plot), suggesting that the mode of rotational motion of PC and PF_6^- changed to overall reorientational motion at ~80°C from the low-temperature small-angle librational motion. Urea showed θ was larger than 360° at the temperature above ~5°C due to the faster -NH_2 group rotation. Similarly, the effective molecular radius, a_T (Figure 1G), was smaller than and similar to the actual size, $a = 0.27$ nm of PF_6^-[24] and PC,[25] at the temperature below and above 80°C, respectively, confirming that the small-angle librational motion at the lower temperatures changed to the overall reorientational motion at $T \geq 80°C$. For urea, $a_T \gg 0.05$ nm for -NH_2 with N–H distance ≈0.1 nm, suggesting that the -NH_2 groups of urea experience a faster localized overall reorientational motion. To verify the lithium-ion transport mechanism at elevated temperature, Li^+ jump distances, d_{Li}, were estimated as a function of temperature (Figure 1H). In E1 at temperatures higher than 80°C, as illustrated in Figure 1I, d_{Li} closes to ~0.9 nm, which corresponds to the distance between the two Li^+ solvation sites sharing one PC molecule in the $[Li(PC)_{4\ or\ 5}]^+$ clusters[23,26–28] with Li^+-O distance of 0.178 nm,[29] suggesting that vehicular transport has ceased for Li^+. Surprisingly, in E2, d_{Li} was reduced to ≤0.45 nm, clearly suggesting that urea additives maintain the vehicular transport of Li^+ at elevated temperatures. It is worth noting that with the increase of temperature, the slopes of ^{1}H $T_{1,PC}$ and $\tau_{c,PC}$ in E0 and E1 (Figure 1D) started to decrease at ~40°C, probably due to the contribution of PC molecules experiencing overall reorientational motion, suggesting that the thermal decomposition reaction in E1 can be facilitated even at $T \approx 40°C$. To clarify this, we measured temperature-dependent ^{1}H T_1 of the ternary mixture of ethylene carbonate/propylene carbonate/ethyl-methyl carbonate (EC/PC/EMC, 4:1:5 wt %) and observed a sharp $T_{1,max}$ at ~40°C (Figure S3), suggesting that $T \approx 40°C$ is a critical point for thermal stability of $LiPF_6$-based carbonate electrolytes and of real LIBs, which are fabricated with electrolytes composed of multiple types of carbonate solvents. Based on the above observations, as illustrated in Figure 1I, we concluded that (1) the first decomposition reaction, $LiPF_6 \rightarrow LiF + PF_5$, was accelerated at elevated temperatures due to the hopping motion of Li^+ assisted by the overall reorientational motion of PC, and (2) urea suppressed the activation of the first decomposition reaction by holding Li^+ inside the solvation cages.

Structural dynamics from AIMD simulations

To gain atomic-level understanding of the effects of temperature and urea addition on structural and dynamics properties correlated with thermal stability of the electrolytes, we performed AIMD simulations for E1 and E2 at 300 and 370 K. Using AIMD trajectories, radial distribution functions (RDFs) and their integrals between Li^+ and O of PC (O_{PC}), F of PF_6^- (F_{PF6}), and O of urea (O_u) were calculated, which

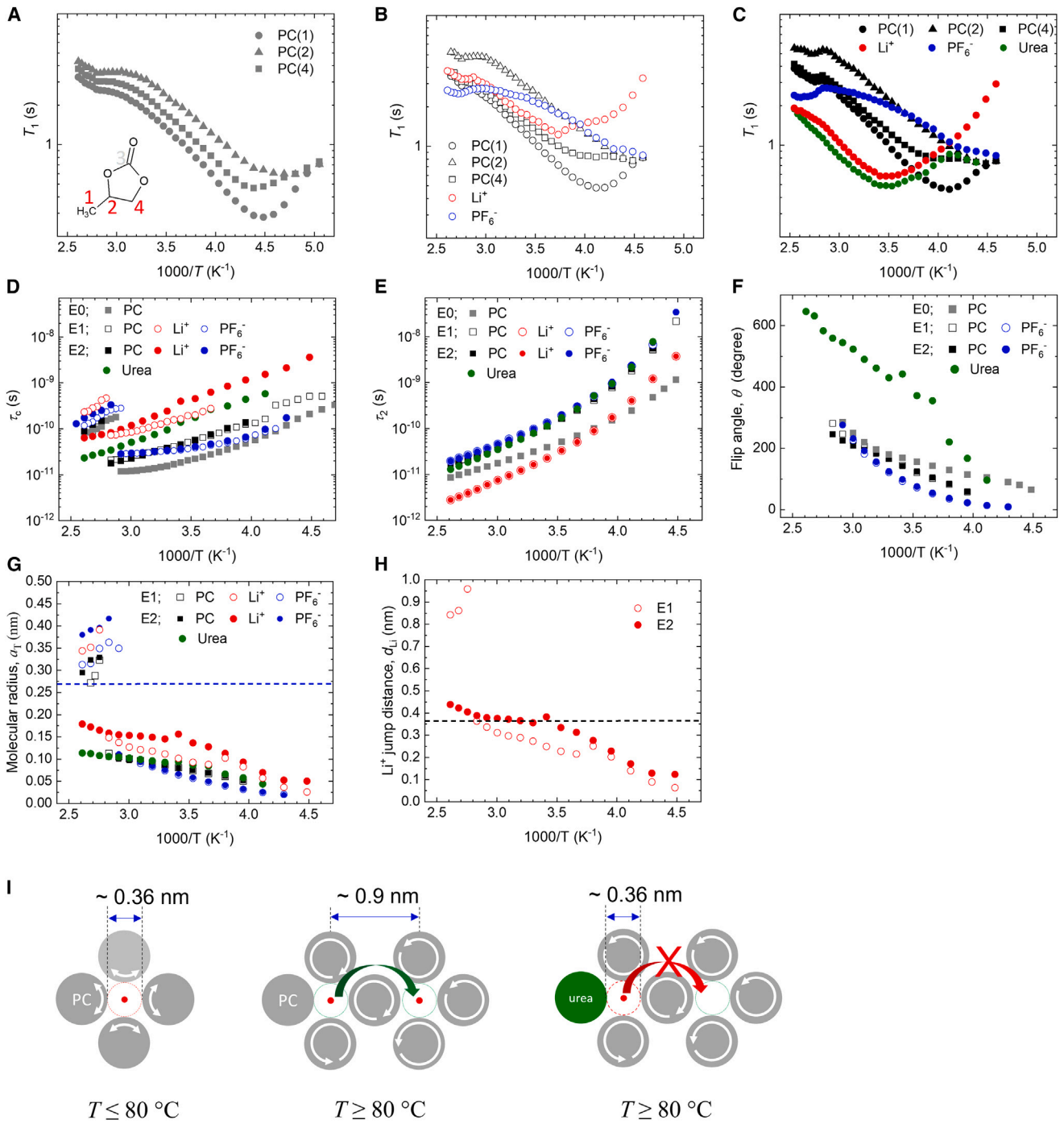

Figure 1. Li$^+$ transport mechanism and electrolyte dynamics

Rotational dynamics of each electrolyte component and Li$^+$ transport mechanism.

(A–E) Temperature-dependent ^{7}Li, ^{19}F, and ^{1}H T_1 for E0 (A), E1 (B), and E2 (C).

(D–H) Temperature-dependent τ_c (D), τ_2 (E), flip angle, θ, (F), apparent molecular radius, a_T, of Li$^+$, PF$_6^-$, PC, and urea (G), and Li$^+$ jump distance, d_{Li} (H).

Schematic of Li$^+$ transport mechanism correlated with the rotational mode of PC with and without urea (I). See experimental procedures section for the details for the calculation of τ_c, τ_2, a_T, and d_{Li}. In the inset of (A), the PC structure with numerals denotes ^{1}H resonance sites. In (B) and (C), the ^{19}F and ^{7}Li T_1 curves, especially in the temperatures lower than the low-temperature $T_{1,min}$, where the T_1 relaxation is less sensitive to the reorientational motion of molecules ($\omega_0\tau_c \gg 1$), were distracted due to the dipolar coupling between ^{19}F-^{1}H and ^{7}Li-^{1}H.[26] In (G), the horizontal line denotes the actual size, $a = 0.27$ nm, for PC and PF$_6^-$. If the τ_c corresponds to small-angle reorientational motion, a_T will be smaller than a.[30] In (H), the horizontal line denotes the estimated diameter (= 0.36 nm) of the Li$^+$ solvation cage in the [Li(PC)$_4$]$^+$ cluster.[29]

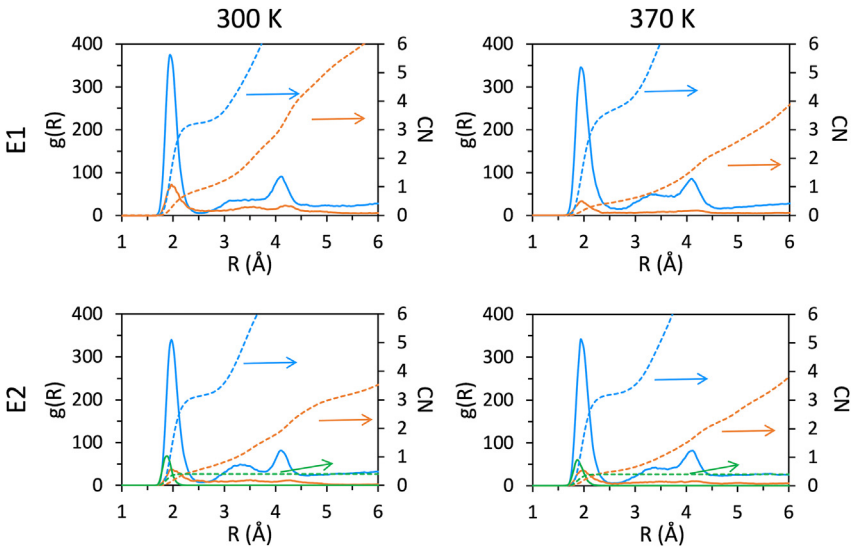

Figure 2. Structural analysis of electrolytes

Radial distribution functions g(R) of Li^+ to O of PC (blue lines), F of PF_6^- (orange lines), and O of urea (green lines).

show the average distance and coordination number (CN) between two species, respectively. Figure 2 shows that distances between Li and O_{PC} (blue line), and Li^+ and F_{PF6} (orange line) are nearly the same (1.93 Å), while in the presence of urea, Li–O_u distance (green line) is 1.87 Å, shorter than Li–O_{PC} and Li–F_{PF6}. This indicates stronger interaction between Li^+ and urea compared with Li^+–PC/Li^+–PF_6^- at both temperatures, which is consistent with the NMR result. Interestingly, unlike similar distances with increased temperatures and urea additive, CN of Li^+ to PF_6^- is decreased by about half at 370 K for urea additive. Although they give overall trends of structural properties, different interactions of each Li^+ with other molecules, especially with PF_6^-, may strongly impact the decomposition of PF_6^-; the performance of LIBs is strongly influenced by chemical stability where interactions between ion-ion and ion-solvent have an important role.[27] Thus, we further analyzed (1) RDFs and CNs for each P with Li^+ (Figure S4), (2) CNs for each Li^+ with PC/PF_6^-/urea molecules without (Figure S5) and with (Figure S6) urea, and (3) the structural details for Li^+ solvation clusters (Figure S7). The general trend observed from these analyses is that the urea additive mitigates the generation of free Li^+/free anions (FI)/solvent-shared monomer and the structural deformation of PF_6^- anions, which is observed from the narrowing of the distribution of the calculated P–F distance probabilities (Figure S8), resulting in improved thermal stability of the electrolyte. Details for these structural analyses can be found in the experimental procedures and supplementary information.

To test the dynamic properties of the electrolyte components, the root mean squared displacements (RMSD) were calculated. The results, presented in Figure S9, show minimal thermal effect on the E2 in contrast to the E1. It is noteworthy that the RMSD of Li^+ at 370 K in E2 plateaued at ~0.3 nm from ~50 ps, while that of E1 reached ~0.5 nm at 70 ps, which exceeds the diameter of the Li^+-solvation sheath (0.37 nm), suggesting that urea additives mitigate thermally activated molecular motion including Li^+ hopping and resulting in stabilizing the Li^+-solvation structures. This finding is consistent with the NMR and structural AIMD analysis above.

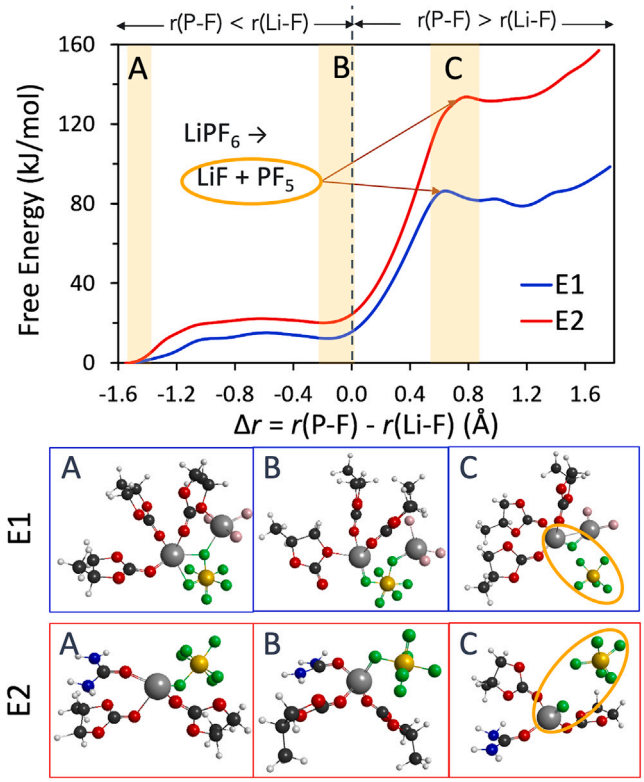

Figure 3. Li-PF_6 decomposition reaction from metadynamics simulations

(Top) Free energy of $LiPF_6$ decomposition forming LiF and PF_5. (Bottom) Structure of each minimum free energy showing as yellow bars labeled A, B, and C.

Li-PF_6 decomposition reaction from metadynamics simulations

As discussed above, the presence of urea hinders the first step of the Li-PF_6 decomposition reaction to form Li-F and PF_5 at elevated temperatures, which may be strongly impacted by structures. To corroborate this, we estimated reaction energy barriers of the first decomposition reaction at 370 K for CID1 (E1) and CUIM (E2) structures by conducting well-tempered metadynamics (MetaD) simulations.[31] Figure 3 shows free energy as a function of distance difference (Δr) between r(P-F) and r(Li-F) where a positive value indicates that Li-F interaction is stronger than that of P-F, along with structures of the three energy minima for both E1 and E2. The structures of the two lower minima show that PF_6^- interacts with 2 Li^+ in the E1 system, in contrast to the E2 system where it interacts with only 1 Li^+. It can be clearly seen that the first decomposition of Li-PF_6 in the E2 system has a free energy barrier more than 1.5 times higher (134 kJ mol^{-1}) than the E1 system (86 kJ mol^{-1}). This difference clearly shows that the decomposition of Li-PF_6 in the presence of urea is both kinetically and thermodynamically unfavorable.

Lithium-ion battery cell test

To confirm the hypothesis that battery performance correlates with the thermal stability of the electrolyte, we conducted comprehensive electrochemical characterizations and gassing behavior analysis (Figure 4). These analyses were performed at an elevated temperature (45°C), which expedites the decomposition of $LiPF_6$. The full cell was fabricated using commercial $LiNi_{0.6}Mn_{0.2}Co_{0.2}O_2$ (NMC622) and $Li_4Ti_5O_{12}$ (LTO) as a cathode and anode electrode, respectively (see experimental procedures

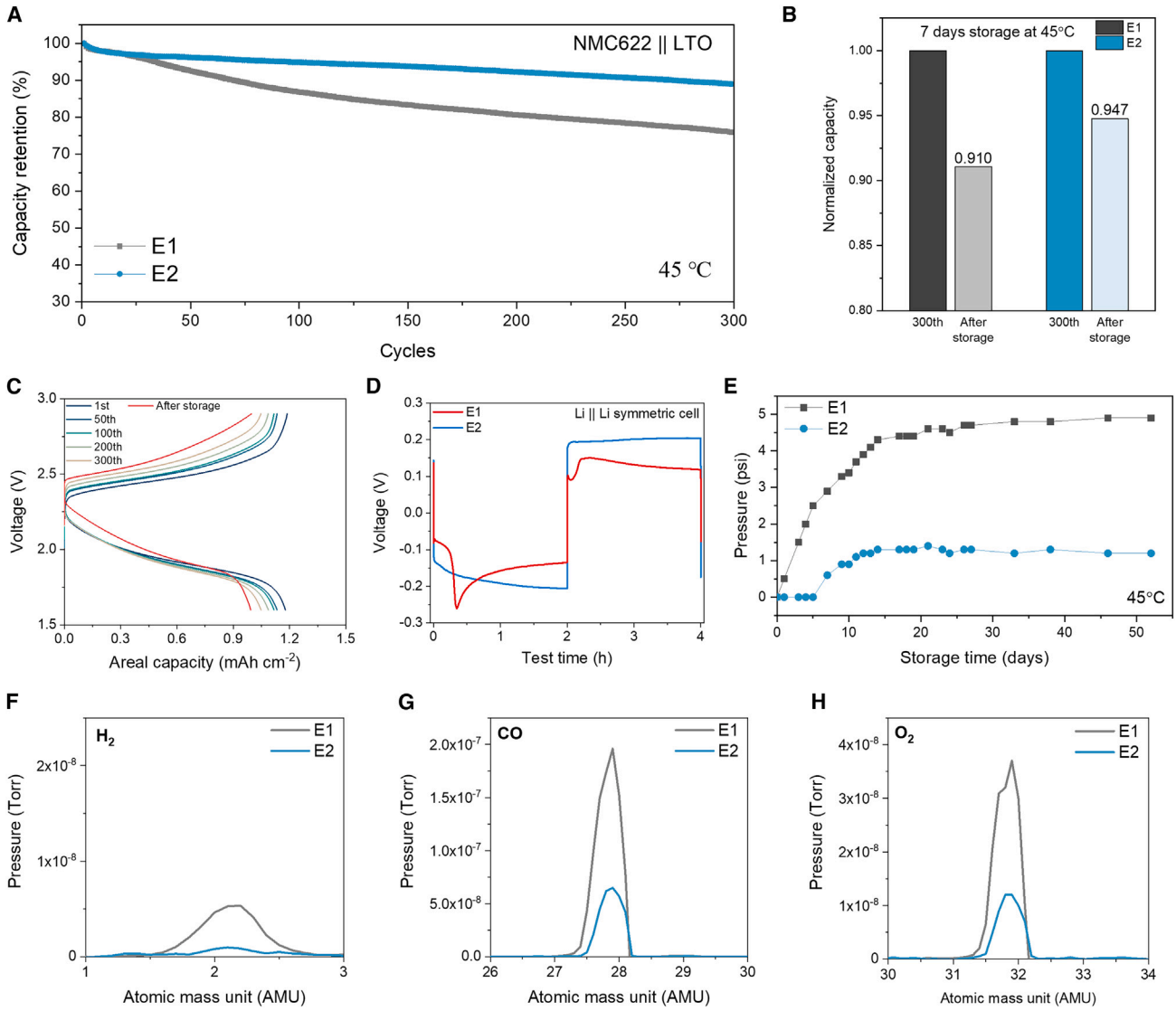

Figure 4. Lithium-ion battery (LIB) cell test

The full cell evaluation at elevated temperature.

(A) Full-cell cycling performance with each electrolyte at elevated temperature (45°C).

(B) Recovery capacity of each cell after 7 days cell aging at 45°C.

(C) Voltage profiles of full cell using E2 electrolyte at each cycle.

(D) Li||Li symmetric cell test for each electrolyte.

(E) Gassing behavior of each full cell assembled by a pressure measurement cell at fully charged state in 45°C for 52 days.

(F–H) Mass spectrometry of the collected gases (hydrogen in F, carbon monoxide in G, and oxygen in H) from the 52 days stored pressure measurement full cells at elevated temperature.

methods). According to the cycling test (Figure 4A), the cell fabricated with E2 (LIB-E2) provided a remarkable capacity retention (89.0%) over 300 cycles, while the cell fabricated with E1 (LIB-E1) has severe capacity degradation with gradual capacity decaying as observed from previously reported NMC||LTO cells.[32] In order to evaluate the aging characteristic of each electrolyte, the cells fabricated with E1 and E2 were stored at an elevated temperature (45°C) for a period of 7 days following 300 cycles (Figure 4B). The LIB-E2 showed a better aging stability with a relatively smaller irreversible capacity loss of 5.3% compared with that of LIB-E1 (9.0%). The voltage

profiles of each cycle confirmed that LIB-E1 had capacity degradation with a relatively large voltage decay, while LIB-E2 provides relatively stable voltage profiles for 300 cycles, even after 7 days of the storage test (Figures 4C and S10). Furthermore, to clarify the interfacial stability of the E2, Li||Li symmetric cells were tested at the temperature of 45°C (Figure 4D). The symmetric cell using E1 electrolyte showed a rapidly increased overpotential with a sharp peak shape during the initial Li stripping process, which is a typical voltage profile of the cell with carbonate electrolytes due to non-uniform kinetics at the Li metal surface.[33,34] In contrast, the symmetric cell using E2 electrolyte, in the initial Li stripping process, exhibited an arc-shaped voltage profile, which generally occurs due to a tortuous Li^+ transport, suggesting the Li^+ transport at the interface is slowed by urea additive that holding Li^+ inside the solvation cage as depicted in Figure 1. These results indicate that the electrochemical stability of LIBs can substantially be improved at elevated temperatures by employing a thermally stabilized electrolyte.[35]

To test the storability of LIBs, we conducted a long-term cell-aging test at 45°C from a fully charged state by monitoring the gassing behavior of LIBs using a pressure measurement cell configuration (Figure 4E). LIB-E1 exhibited a rapidly increased gas generation at an early stage of the aging, which stabilized around 4.5 psi after 14 days. In contrast, LIB-E2 showed a mitigated gassing behavior (1.2 psi) with a smooth increase and stabilization after 14 days of aging. For the details of the gassing behavior, mass spectrometry was performed with the collected gases from pressure measurement cells for both LIB-E1 and LIB-E2 (Figures 4F–4H), and the whole spectra of mass spectrometry are shown in Figure S11. The evolutions of H_2 (Figure 4F), CO (Figure 4G), and O_2 (Figure 4H) gases, which can be generated due to the electrolyte decomposition (H_2 and CO)[36–38] and from a lattice of layered oxide cathode (O_2),[39,40] was noticeably smaller in LIB-E2 compared with LIB-E1, implying the superior storability (i.e., calendar life) of LIB fabricated with E2. This observation strongly suggests that the calendar life of LIBs can effectively be extended by using a thermally stabilized electrolyte such as E2.

This study confirmed that high-temperature Li^+ hopping, assisted by the overall reorientational motion of solvent molecules, is responsible for the activation of the decomposition of $LiPF_6$ in a $LiPF_6$-based carbonate electrolyte at elevated temperatures. AIMD calculations showed that the strong interaction of urea can suppress thermally activated molecular motion, including Li^+ hopping, resulting in higher structural stability of Li^+ solvation clusters and PF_6^- anions and a higher free energy barrier for the $LiPF_6$ decomposition reaction at elevated temperatures. Electrochemical characterization including long-term cell-aging test and gassing behavior analysis at 45°C performed with NMC||LTO cells showed a superior cycle and storage performance with the urea-added electrolyte. This work provides a new strategy: suppressing Li^+ hopping at elevated temperature to design thermally stable $LiPF_6$-based carbonate electrolytes, enabling thermally stable LIBs with improved cycle and calendar life even at elevated temperatures.

EXPERIMENTAL PROCEDURES

Resource availability

Lead contact

Further information and requests for resources should be directed to and will be fulfilled by the lead contact, Kee Sung Han (keesung.han@pnnl.gov).

Materials availability

This study did not generate new unique materials.

Data and code availability

The data presented in this work are available from the corresponding authors upon reasonable request. This study did not generate any code.

Sample preparation

Battery-grade 1 M $LiPF_6$ in PC solvent (Sigma-Aldrich) was used as E1 electrolyte, and 2 wt % of urea (99.0%–100.5%, Sigma-Aldrich) was added to prepare the urea-containing E2 electrolyte.

Diffusion and spin-lattice relaxation time measurements

Diffusion coefficient and T_1 relaxation measurements were performed on a 600-MHz (^{1}H NMR frequency at 14.1 T) NMR spectrometer (Agilent, USA) equipped with a 5-mm liquid NMR probe (Doty Scientific, USA) at the frequencies of 599.379, 563.937, and 232.940 MHz, respectively, for ^{1}H, ^{19}F, and ^{7}Li. Temperature-dependent diffusion coefficients of PC molecules, PF_6^- anions, and Li^+ cations for all samples in the temperature range of −50°C to 110°C were measured by ^{1}H, ^{19}F, and ^{7}Li PFG NMR using the stimulated echo sequence (Dbppste, VNMRJ, Agilent, USA) with the 90° pulse lengths of 11, 16, and 8.5 μs for ^{1}H, ^{19}F, and ^{7}Li, respectively. The PFG-echo profile obtained as a function of gradient strength (g) was fitted with the Stejskal-Tanner equation[41]:

$$S(g) = S(0)exp\left[-D(\gamma\delta g)^2(\Delta - \delta/3)\right], \quad \text{(Equation 1)}$$

where the echo intensities S(g) and S(0) are at a gradient strength of g and 0, respectively. D, γ, δ, and Δ are diffusion coefficient, gyromagnetic ratio for observing nucleus, $\gamma(^1H) = 2\pi \times 42.576$, $\gamma(^{19}F) = 2\pi \times 40.052$, and $\gamma(^7Li) = 2\pi \times 42.576$ rad•MHz•T^{-1}, gradient length, and diffusion delay, which is the duration between the two bipolar gradient pairs, respectively. For all diffusion measurements, δ and Δ were fixed at 2 ms and 50 ms, respectively. Temperature-dependent ^{1}H, ^{19}F, and ^{7}Li T_1 in the temperature range of −50°C to 110°C were obtained using the inversion recovery (180° – τ – 90° – *acquire*).

Usually, the diffusion coefficient is inversely proportional to viscosity of solution as predicted by the Stokes-Einstein equation: $D = k_BT/6\pi\eta r_s$, where D is diffusion coefficient, k_B is the Boltzmann constant, T is the absolute temperature, η is viscosity, and r_s is the hydrodynamic radius of diffusing molecule. The diffusional behavior can be studied using the VFT equation, $D = D_0 \cdot \exp(-B/(T-T_0))$, where D_0, B, and T_0 are adjustable parameters and the translational activation energy, E_a, that can be calculated using the Arrhenius equation, $D = D_0 \cdot \exp(-E_a/RT)$, where D_0 is the fitting parameter, R is the gas constant, and T is the absolute temperature.

For determination of rotational correlation times, τ_c

The rotational correlation times of each component, PC, PF_6^-, and Li^+, of the electrolyte were estimated from temperature-dependent ^{1}H, ^{19}F, and ^{7}Li T_1 relaxation times using the Bloembergen-Purcell-Pound equation[42]:

$$\frac{1}{T_1} = C\left[\frac{\tau_c}{1+\omega_0^2\tau_c^2} + \frac{4\tau_c}{1+4\omega_0^2\tau_c^2}\right], \quad \text{(Equation 2)}$$

where $\omega_0 = 2\pi\nu_0$ (rad·s^{-1}) with ν_0 is the observed frequency, and τ_c is the rotational correlation time. The $\nu_0(^1H)$, $\nu_0(^{19}F)$, and $\nu_0(^7Li)$ are 599.379, 563.93, and 232.940 MHz, respectively. For ^{1}H and ^{19}F T_1 relaxations, which occur mainly via the

dipole-dipole interactions between protons/fluorine in the same site, C in Equation 2 can be written as follows:

$$C_d = \frac{2}{5}\left(\frac{\mu_0}{4\pi}\right)^2 \gamma^4 \hbar^2 \sum r_{ij}^{-6} I(I+1), \quad \text{(Equation 3)}$$

where μ_0 is the vacuum permeability, γ is the gyromagnetic ratio of observing nucleus, such as $\gamma(^1H) = 2\pi \times 42.576$ rad•MHz•T^{-1} and $\gamma(^{19}F) = 2\pi \times 40.052$ rad•MHz•T^{-1}, $\hbar$ is reduced Plank's constant, r_{ij} is the distance between protons/fluorine that is dipolar coupled to the proton/fluorine evaluated, and I is nuclear spin number of the proton/fluorine ($I = 1/2$). While ^{7}Li ($I = 3/2$) T_1 relaxation occurs mainly due to the quadrupolar interaction, C in Equation 2 can be correlated with the quadrupolar coupling constant, $\omega_q = 2\pi\nu_q$, as follows[43,44]:

$$C_q = \frac{{\omega_q}^2}{50} \quad \text{(Equation 4)}$$

Using the fact that $\omega_0\tau_c = 2\pi\nu_0\tau_c \approx 0.616$ at the T_1 minimum ($T_{1,min}$), unknown parameters $\sum r_{ij}^{-6}$ and ω_q in C_d and C_q, respectively, can experimentally be determined both for high- and low-temperature $T_{1,min}$. Then, it is possible to estimate the rotational correlation time for all measured T_1 values. At the $T_{1,min}$, the rotational correlation times, τ_c, for ^{1}H, ^{19}F, and ^{7}Li will be 1.63×10^{-10} (163 ps), 1.74×10^{-10} (174 ps), and 4.21×10^{-10} s (421 ps), respectively, in this study, under the external magnetic field intensity of 14.1 T.

For determination of overall isotropic reorientational correlation times, τ_2

We estimated overall isotropic reorientational correlation time, τ_2, using the Stokes-Einstein-Debye relation as follows[44,45]:

$$\tau_2 = \frac{V\eta}{k_B T}, \quad \text{(Equation 5)}$$

where V is the volume of a molecule, η is the viscosity, k_B is the Boltzmann constant, and T is absolute temperature. In actual calculations, we used measured diffusion coefficients, D ($=k_BT/c\pi\eta a$), where a is the radius of diffusing molecule, and c is 6 in the stick boundary condition. Then Equation 5 could be written as follows[44,45]:

$$\tau_2 = \frac{4a^2}{3cD} \quad \text{(Equation 6)}$$

Here, the molecular radius $a = 0.27$ nm for both PF_6^- anion[24] and PC molecule,[25] and $a \approx 0.18$ nm for urea. The temperature-dependent flip angle of PC molecules was estimated using the τ_c and τ_2 obtained from the PC(4) site.

For determination of flip angles, θ

We calculated the flip angles, θ, of PC and PF_6^- in each solution as a function of temperature from the estimated rotational correlation time, τ_c, and overall isotropic reorientational correlation time, τ_2, using the Stokes-Einstein-Debye relation as follows[44,45]:

$$\theta = \frac{360\cdot\tau_c}{\tau_2} \quad \text{(Equation 7)}$$

For estimation of apparent molecular radius, a_T

The apparent molecular radii, a_T, were estimated using the following relation[43]:

$$a_T = \sqrt{\tau_c D} \quad \text{(Equation 8)}$$

While, in Equation 8, D should be the rotational diffusion coefficient according to the Stokes-Einstein-Debye relationship, in this study, translation diffusion coefficients were used for the rough estimation of the molecular radius for the elucidation of

molecular motion. The estimated a_T will be smaller than the actual radius of the molecules if the molecule experiences a librational motion.

For estimation of lithium jump distance, d_{Li}, to obtain the information for the Li^+ cation translational mechanism, the jump distance, d, of a single Li^+ ion was estimated using the follow relation[43]:

$$d_{Li} = \sqrt{6\tau_c D} \quad \text{(Equation 9)}$$

AIMD simulations

To determine the local structure and their dynamics at a given temperature, model systems were generated consisting of PC and $LiPF_6$ in the absence and presence of urea following the experimental compositions of E1 and E2 samples with a 20-Å cubic box. Periodic density functional theory (DFT)-based AIMD simulations were carried out within the generalized gradient approximation with Perdew, Burke, and Ernzerhof exchange-correlation functionals[46] and Grimme's third-generation (DFT-D3)[47] for dispersion correction as implemented in the CP2K package.[48,49] Goedecker-Teter-Hutter pseudopotentials are used for the core electrons,[50] while the valence wave functions are expanded in terms of double-ζ quality basis sets optimized for condensed systems to minimize linear dependencies and superposition errors. Electrostatic terms are calculated using an additional auxiliary plane-wave basis set with a 400-Ry cutoff. The Γ-point approximation is employed for the Brillouin zone integration because of the significant size of the supercell.

AIMD simulations are performed within the canonical NVT ensemble using a 0.5-fs time step and a Nosé-Hoover thermostat chain at 300 and 370 K. Each system was thermalized for at least 30 ps, and then well-equilibrated trajectories of >20 ps were collected to obtain reliable statistical properties.

Metadynamics simulations

We employed *ab initio* well-tempered metadynamics simulations[31] implemented in the PLUMED2 code[51] in combination with CP2K package. Gaussian hills with an initial height of 3.0 kJ mol^{-1} and $\boldsymbol{\sigma}$ = 0.15 were deposited every 100 time steps with a bias factor of 50 along the collective variable (CV). For each simulation, we ran 50 ps after equilibration (~25 ps) with a 0.5-fs time step. For the CV, we considered the distance difference (Δr) between P-F and Li-F, i.e., $\Delta r = r$(P-F) – r(Li-F) in the form of an anti-symmetric linear combination where Δr is limited from −6 to 6 Å. The error associated with this procedure is lower than 2 kJ mol^{-1}.

Electrochemical measurements

For the electrochemical measurements, it is well known that NMC622 and LTO electrode materials can provide an excellent cycling performance at room-temperature cell operation due to their good structural stability. For this reason, in this work, we fabricated a full cell using these electrode materials to focus solely on the electrolyte affecting the battery performance by minimizing the side reactions derived from the electrode material degradations. The cathode electrode was fabricated using commercial NCM622, the carbon black (Super P, TIMCAL), and polyvinylidene fluoride binder (PVdF, Kureha) with a mass ratio of 96:2:2 on the aluminum foil. Electrode porosity and mass loading level of the cathode were 30.0% and 10.0 mg cm^{-2}, respectively. For the anode, commercial LTO, Super P, and PVdF were mixed with a mass ratio of 94:3:3 on the aluminum foil. Electrode density and mass loading level of the anode were 35.0% and 10.0 mg cm^{-2}, respectively. The negative/positive capacity ratio (N/P ratio) was fixed at 1.1 for all tests. Each electrode was punched into

15 mm diameter for the coin-type full cell fabrication with 1.0 mAh of cell capacity. The coin-type full cells were assembled in the Ar-filled glovebox (H_2O < 0.1 ppm, O_2 < 0.1 ppm) with E1 and E2 electrolyte. The electrochemical tests were evaluated in a voltage range between 2.9 and 1.6 V at a 0.2 C-rate at the first cycle and 0.5 C-rate for the rest of the cycles. All electrochemical evaluations were performed by a battery tester (Arbin). The aging test was conducted by storing each cell in an isothermal chamber (45°C) at a fully discharged state for 7 days.

For the Li||Li symmetric cell evaluation, the coin-type cell was fabricated in the Ar-filled glovebox with Li chip (16 mm diameter, 250 mm thick, MSE supplies) as both the reference and counter electrode. The Li||Li symmetric cells were evaluated at 0.5 mA cm^{-2} for 2 h of Li plating/stripping process.

Storage test with gassing behavior analysis

The cell for storage test was fabricated using a commercial pressure measurement cell (MTI) with the same cathode and anode electrode. The pressure measurement cells were assembled in the Ar-filled glovebox (H_2O < 0.1 ppm, O_2 < 0.1 ppm) with E1 and E2 electrolyte, respectively. These pressure cells were performed in the first cycle with 0.1 C-rate and fully charged at 2.9 V with 0.1 C-rate at room temperature. Then, the fully charged pressure cells were placed in an isothermal chamber (45°C) over 50 days. We manually recorded the gas pressure of each cell. To analyze the composition of gas generated for the cell storage, mass spectroscopy (RGA 200, Stanford Research System) for gas analysis was conducted after 52 days of cell aging.

SUPPLEMENTAL INFORMATION

Supplemental information can be found online at https://doi.org/10.1016/j.xcrp.2023.101768.

ACKNOWLEDGMENTS

This work was conducted under the Laboratory Directed Research and Development Program (LDRD) at Pacific Northwest National Laboratory (PNNL), a multiprogram national laboratory operated by Battelle for the US Department of Energy under Contract DE-AC05-76RL01830. This work was also partly supported by the US Department of Energy (DOE), Office of Science, Office of Basic Energy Sciences, Division of Chemical Sciences, and Geosciences & Biosciences (FWP 47319) and the US Department of Energy (DOE) Office of Electricity (OE) under contract no. 57558. We are also grateful for guidance provided by Dr. Imre Gyuk, the program manager of the Energy Storage and Power Electronics Program at DOE-OE. The NMR measurements were performed at the Environmental Molecular Sciences Laboratory (EMSL), a national scientific user facility sponsored by the Department of Energy's Office of Biological and Environmental Research and located at PNNL, and partially supported by the Joint Center for Energy Storage Research (JCESR), an Energy Innovation Hub funded by the US Department of Energy, Office of Science, Basic Energy Sciences. Computational resources were provided by the PNNL Research Computing facility and the National Energy Research Scientific Computing Center (NERSC), a US Department of Energy Office of Science User Facility located at Lawrence Berkeley National Laboratory (LBNL).

AUTHOR CONTRIBUTIONS

Conceptualization, K.S.H.; investigation, K.S.H., M.-S.L., N.K., D.C., S.C., J.R., G.P., R.R., and E.C.T.; writing – original draft, K.S.H, M.-S.L., and N.K.; writing – review & editing,

K.S.H., M.-S.L, D.C., and N.K.; funding acquisition, K.S.H., M.-S.L., and D.C.; supervision, K.S.H.

DECLARATION OF INTERESTS

The authors declare no conflict of interest.

Received: September 18, 2023
Revised: November 6, 2023
Accepted: December 11, 2023
Published: January 5, 2024

REFERENCES

1. Xu, K. (2004). Nonaqueous liquid electrolytes for lithium-based rechargeable batteries. Chem. Rev. *104*, 4303–4417.

2. Choi, D., Shamim, N., Crawford, A., Huang, Q., Vartanian, C.K., Viswanathan, V.V., Paiss, M.D., Alam, M.J.E., Reed, D.M., and Sprenkle, V.L. (2021). Li-ion battery technology for grid application. J. Power Sources *511*, 230419.

3. Rodrigues, M.-T.F., Babu, G., Gullapalli, H., Kalaga, K., Sayed, F.N., Kato, K., Joyner, J., and Ajayan, P.M. (2017). A materials perspective on Li-ion batteries at extreme temperatures. Nat. Energy *2*, 17108.

4. He, Y.-B., Li, B., Liu, M., Zhang, C., Lv, W., Yang, C., Li, J., Du, H., Zhang, B., Yang, Q.-H., et al. (2012). Gassing in $Li_4Ti_5O_{12}$-based batteries and its remedy. Sci. Rep. *2*, 913.

5. Duan, J., Tang, X., Dai, H., Yang, Y., Wu, W., Wei, X., and Huang, Y. (2020). Building safe lithium-ion batteries for electric vehicles: a review. Electrochem. Energy Rev. *3*, 1–42.

6. Janek, J., and Zeier, W.G. (2016). A solid future for battery development. Nat. Energy *1*, 16141.

7. Kim, N., Shamim, N., Crawford, A., Viswanathan, V.V., Sivakumar, B.M., Huang, Q., Reed, D., Sprenkle, V., and Choi, D. (2022). Comparison of Li-ion battery chemistries under grid duty cycles. J. Power Sources *546*, 231949.

8. Leng, F., Tan, C.M., and Pecht, M. (2015). Effect of temperature on the aging rate of Li ion battery operating above room temperature. Sci. Rep. *5*, 12967.

9. Liu, K., Liu, Y., Lin, D., Pei, A., and Cui, Y. (2018). Materials for lithium-ion battery safety. Sci. Adv. *4*, eaas9820.

10. Fan, X., Ji, X., Chen, L., Chen, J., Deng, T., Han, F., Yue, J., Piao, N., Wang, R., Zhou, X., et al. (2019). All-temperature batteries enabled by fluorinated electrolytes with non-polar solvents. Nat. Energy *4*, 882–890.

11. Tasaki, K., Kanda, K., Nakamura, S., and Ue, M. (2003). Decomposition of $LiPF_6$ and stability of PF_5 in Li-ion battery electrolytes. J. Electrochem. Soc. *150*, A1628.

12. Wilken, S., Treskow, M., Scheers, J., Johansson, P., and Jacobsson, P. (2013). Initial stages of thermal decomposition of $LiPF_6$-based lithium ion battery electrolytes by detailed Raman and NMR spectroscopy. RSC Adv. *3*, 16359–16364.

13. Henschel, J., Peschel, C., Klein, S., Horsthemke, F., Winter, M., and Nowak, S. (2020). Clarification of decomposition pathways in a state-of-the-art lithium ion battery electrolyte through ^{13}C-Labeling of electrolyte components. Angew. Chem. Int. Ed. *59*, 6128–6137.

14. Yang, H., Zhuang, G.V., and Ross, P.N. (2006). Thermal stability of $LiPF_6$ salt and Li-ion battery electrolytes containing $LiPF_6$. J. Power Sources *161*, 573–579.

15. Campion, C.L., Li, W., and Lucht, B.L. (2005). Thermal decomposition of $LiPF_6$-based electrolytes for lithium-ion batteries. J. Electrochem. Soc. *152*, A2327–A2334.

16. Zinigrad, E., Larush-Asraf, L., Gnanaraj, J.S., Sprecher, M., and Aurbach, D. (2005). On the thermal stability of $LiPF_6$. Thermochim. Acta *438*, 184–191.

17. Li, W., Campion, C., Lucht, B.L., Ravdel, B., DiCarlo, J., and Abraham, K.M. (2005). Additives for stabilizing $LiPF_6$-based electrolytes against thermal decomposition. J. Electrochem. Soc. *152*, A1361.

18. Stich, M., Göttlinger, M., Kurniawan, M., Schmidt, U., and Bund, A. (2018). Hydrolysis of $LiPF_6$ in carbonate-based electrolytes for lithium-ion batteries and in aqueous media. J. Phys. Chem. C *122*, 8836–8842.

19. Haregewoin, A.M., Wotango, A.S., and Hwang, B.-J. (2016). Electrolyte additives for lithium ion battery electrodes: progress and perspectives. Energy Environ. Sci. *9*, 1955–1988.

20. Nandy, A., and Smiatek, J. (2019). Mixtures of LiTFSI and urea: ideal thermodynamic behavior as key to the formation of deep eutectic solvents? Phys. Chem. Chem. Phys. *21*, 12279–12287.

21. Liang, H., Li, H., Wang, Z., Wu, F., Chen, L., and Huang, X. (2001). New binary room-temperature molten salt electrolyte based on urea and LiTFSI. J. Phys. Chem. B *105*, 9966–9969.

22. Ogawa, H., and Mori, H. (2020). Lithium salt/amide-based deep eutectic electrolytes for lithium-ion batteries: electrochemical, thermal and computational study. Phys. Chem. Chem. Phys. *22*, 8853–8863.

23. Self, J., Fong, K.D., and Persson, K.A. (2019). Transport in superconcentrated $LiPF_6$ and $LiBF_4$/propylene carbonate electrolytes. ACS Energy Lett. *4*, 2843–2849.

24. Johansson, P. (2007). Electronic structure calculations on lithium battery electrolyte salts. Phys. Chem. Chem. Phys. *9*, 1493–1498.

25. Marcus, Y. (1998). The Properties of Solvents (Wiley).

26. Kumar, V., Reddy, R.R., Kumar, B.V.N.P., Avadhani, C.V., Ganapathy, S., Chandrakumar, N., and Sivaram, S. (2019). Lithium speciation in the $LiPF_6$/PC electrolyte studied by two-dimensional heteronuclear overhauser enhancement and pulse-field gradient diffusometry NMR. J. Phys. Chem. C *123*, 9661–9672.

27. Hwang, S., Kim, D.-H., Shin, J.H., Jang, J.E., Ahn, K.H., Lee, C., and Lee, H. (2018). Ionic conduction and solution structure in $LiPF_6$ and $LiBF_4$ propylene carbonate electrolytes. J. Phys. Chem. C *122*, 19438–19446.

28. Kondo, K., Sano, M., Hiwara, A., Omi, T., Fujita, M., Kuwae, A., Iida, M., Mogi, K., and Yokoyama, H. (2000). Conductivity and solvation of Li^+ Ions of $LiPF_6$ in propylene carbonate solutions. J. Phys. Chem. B *104*, 5040–5044.

29. Skarmoutsos, I., Ponnuchamy, V., Vetere, V., and Mossa, S. (2015). Li^+ solvation in pure, binary, and ternary mixtures of organic carbonate electrolytes. J. Phys. Chem. C *119*, 4502–4515.

30. Qi, F., Schug, K.U., Dupont, S., Döß, A., Böhmer, R., Sillescu, H., Kolshorn, H., and Zimmermann, H. (2000). Structural relaxation of the fragile glass-former propylene carbonate studied by nuclear magnetic resonance. J. Chem. Phys. *112*, 9455–9462.

31. Barducci, A., Bussi, G., and Parrinello, M. (2008). Well-tempered metadynamics: a smoothly converging and tunable free-energy method. Phys. Rev. Lett. *100*, 020603.

32. Björklund, E., Naylor, A.J., Brant, W., Brandell, D., Younesi, R., and Edström, K. (2019). Temperature dependence of electrochemical degradation in $LiNi_{1/3}Mn_{1/3}Co_{1/3}O_2/Li_4Ti_5O_{12}$ cells. Energ. Tech. *7*, 1900310.

33. Bieker, G., Winter, M., and Bieker, P. (2015). Electrochemical in situ investigations of SEI and dendrite formation on the lithium metal anode. Phys. Chem. Chem. Phys. *17*, 8670–8679.

34. Chen, K.-H., Wood, K.N., Kazyak, E., LePage, W.S., Davis, A.L., Sanchez, A.J., and Dasgupta, N.P. (2017). Dead lithium: mass transport

effects on voltage, capacity, and failure of lithium metal anodes. J. Mater. Chem. A *5*, 11671–11681.

35. Kim, H.S., Verma, R., Kim, J., and Park, C.J. (2020). Effect of urea as electrolyte additive for stabilization of lithium metal electrodes. ACS Sustain. Chem. Eng. *8*, 11123–11132.

36. Zhang, B., Metzger, M., Solchenbach, S., Payne, M., Meini, S., Gasteiger, H.A., Garsuch, A., and Lucht, B.L. (2015). Role of 1,3-propane sultone and vinylene carbonate in solid electrolyte interface formation and gas generation. J. Phys. Chem. C *119*, 11337–11348.

37. Lv, W., Gu, J., Niu, Y., Wen, K., and He, W. (2017). Review-gassing mechanism and suppressing solutions in $Li_4Ti_5O_{12}$-based lithium-ion batteries. J. Electrochem. Soc. *164*, A2213–A2224.

38. Liu, J., Bian, P., Li, J., Ji, W., Hao, H., and Yu, A. (2015). Gassing behavior of lithium titanate based lithium ion batteries with different types of electrolytes. J. Power Sources *286*, 380–387.

39. Yang, L., Ravdel, B., and Lucht, B.L. (2010). Electrolyte reactions with the surface of high voltage $LiNi_{0.5}Mn_{1.5}O_4$ cathodes for lithium-ion batteries. Electrochem. Solid State Lett. *13*, A95.

40. Wu, K., Yang, J., Liu, Y., Zhang, Y., Wang, C., Xu, J., Ning, F., and Wang, D. (2013). Investigation on gas generation of $Li_4Ti_5O_{12}$/$LiNi_{1/3}Co_{1/3}Mn_{1/3}O_2$ cells at elevated temperature. J. Power Sources *237*, 285–290.

41. Stejskal, E.O., and Tanner, J.E. (1965). Spin diffusion measurements: spin echoes in the presence of a time-dependent field gradient. J. Chem. Phys. *42*, 288–292.

42. L Sudmeier, J., E Anderson, S., S Frye, J., Frye, S., and J.. (1990). Calculation of nuclear spin relaxation times. Concepts Magn. Reson. *2*, 197–212.

43. Hayamizu, K., Tsuzuki, S., Seki, S., Ohno, Y., Miyashiro, H., and Kobayashi, Y. (2008). Quaternary ammonium room-temperature ionic liquid including an oxygen atom in side chain/lithium salt binary electrolytes: ionic conductivity and ^{1}H, ^{7}Li, and ^{19}F NMR studies on diffusion coefficients and local motions. J. Phys. Chem. B *112*, 1189–1197.

44. Hayamizu, K., Tsuzuki, S., Seki, S., Fujii, K., Suenaga, M., and Umebayashi, Y. (2010). Studies on the translational and rotational motions of ionic liquids composed of N-methyl-N-propyl-pyrrolidinium (P_{13}) cation and bis(trifluoromethanesulfonyl)amide and bis(fluorosulfonyl)amide anions and their binary systems including lithium salts. J. Chem. Phys. *133*, 194505.

45. Hayamizu, K., Tsuzuki, S., and Seki, S. (2008). Molecular motions and ion diffusions of the room-temperature ionic liquid 1,2-dimethyl-3-propylimidazolium bis(trifluoromethylsulfonyl)amide (DMPImTFSA) Studied by ^{1}H, ^{13}C, and ^{19}F NMR. J. Phys. Chem. A *112*, 12027–12036.

46. Perdew, J.P., Burke, K., and Ernzerhof, M. (1996). Generalized gradient approximation made simple. Phys. Rev. Lett. *77*, 3865–3868.

47. Grimme, S., Antony, J., Ehrlich, S., and Krieg, H. (2010). A consistent and accurate ab initio parametrization of density functional dispersion correction (DFT-D) for the 94 elements H-Pu. J. Chem. Phys. *132*, 154104.

48. Kühne, T.D., Iannuzzi, M., Del Ben, M., Rybkin, V.V., Seewald, P., Stein, F., Laino, T., Khaliullin, R.Z., Schütt, O., Schiffmann, F., et al. (2020). CP2K: An electronic structure and molecular dynamics software package - Quickstep: Efficient and accurate electronic structure calculations. J. Chem. Phys. *152*, 194103.

49. VandeVondele, J., Krack, M., Mohamed, F., Parrinello, M., Chassaing, T., and Hutter, J. (2005). Quickstep: Fast and accurate density functional calculations using a mixed Gaussian and plane waves approach. Comput. Phys. Commun. *167*, 103–128.

50. Goedecker, S., Teter, M., and Hutter, J. (1996). Separable dual-space Gaussian pseudopotentials. Phys. Rev. B *54*, 1703–1710.

51. PLUMED consortium, Bussi, G., Camilloni, C., Tribello, G.A., Banáš, P., Barducci, A., Bernetti, M., Bolhuis, P.G., Bottaro, S., Branduardi, D., et al. (2019). Promoting transparency and reproducibility in enhanced molecular simulations. Nat. Methods *16*, 670–673.